

Adsorption of volatiles on dust grains in protoplanetary disks

LILE WANG ,^{1, 2} FENG LONG ,^{1, 2} HAIFENG YANG ,^{3, 4} RUOBING DONG ,¹ AND SHENZHEN XU ,⁵

¹ *Kavli Institute for Astronomy and Astrophysics, Peking University, Beijing 100871, China*

² *Department of Astronomy, School of Physics, Peking University, Beijing 100871, China*

³ *Institute for Astronomy, School of Physics, Zhejiang University, 886 Yuhangtang Road, Hangzhou 310027, China*

⁴ *Center for Cosmology and Computational Astrophysics, Institute for Advanced Study in Physics, Zhejiang University, Hangzhou 310027, China*

⁵ *School of Material Sciences, Peking University, Beijing 100871, China*

ABSTRACT

The adsorption of volatile molecules onto dust grain surfaces fundamentally influences dust-related processes, including condensation of gas-phase molecules, dust coagulation, and planet formation in protoplanetary disks. Using advanced *ab-initio* density functional theory with r²SCAN+rVV10 van der Waals functionals, we calculate adsorption energies of H₂, H₂O, and CO on carbonaceous (graphene, amorphous carbon) and silicate (MgSiO₃) surfaces. Results reveal fundamentally different adsorption mechanisms: weak physisorption on carbonaceous surfaces ($|\Delta\epsilon_{\text{ad}}| \sim 0.1 - 0.2$ eV) versus strong chemisorption on silicates ($|\Delta\epsilon_{\text{ad}}| \sim 0.5 - 1.5$ eV) via coordination bonds. Kinetic Monte Carlo simulations incorporating these energies demonstrate divergent surface evolution: carbonaceous grains exhibit distinct condensation radius compared to silicates, while the cocrystal of H₂O and CO significantly increases the desorption temperature of CO. The actual radii of gas-phase molecule depletion could thus be a comprehensive result of temperatures, chemical compositions, and even evolution tracks. Meanwhile, silicates maintain chemisorbed molecular coatings throughout most disk regions. Such dichotomy in surface coverage could also provide a natural mechanism for carbon depletion in inner planetary systems.

Keywords: Protoplanetary disks(1300), Exoplanet formation (492), Interstellar dust (836), Dust physics (2229), Astrophysical dust processes (99)

1. INTRODUCTION

The adsorption of volatile chemical species onto the surfaces of dust grains is of broad and critical interest to researchers studying the interstellar medium (ISM), star formation, and planet formation. For example, in protoplanetary disks (PPDs hereafter), dusts may play a central role in controlling the thermochemical conditions. Grains also hold the chemical equilibrium of formation versus dissociation inside disks, as their surfaces are the places where most H₂ and H₂O are formed (e.g. Cazaux & Tielens 2002, 2004; Ádámkovics et al. 2014). Moreover, dust surfaces can adsorb gas-phase charge carriers (ions and free electrons) rather efficiently, letting these carriers deposit their free charge and get neutralized as they get desorbed (e.g. Ilgner & Nelson 2006; see also Bai & Goodman 2009). This mechanism maintains a low but non-zero fraction of ionization in the pertinent zones in PPDs, enabling the non-ideal magnetohydrodynamic (MHD) effects to drive disk winds and accretion flows efficiently (Bai & Goodman 2009; Bai 2011, 2017; Wang et al. 2019). Volatile coatings on dust grain surfaces, for example water, regulate grain sintering and thereby shape the dust size distribution throughout PPD evolution (Okuzumi et al. 2016; Hasegawa et al. 2017). Such modulated distributions could influence their interactions with charged particles and lead to the formation of sub-structures in PPDs by alternating the magnetic diffusivities, the key parameters determining the interactions between the magnetic fields and the gas (e.g. Hu et al. 2019, 2021). More generally, the dynamic events related to dust growth, including coagulation, bouncing, breaking, and shattering of grains, are sensitively dependent on the sticking energy between surfaces (Chokshi et al. 1993; Dominik &

2006; see also Bai & Goodman 2009). This mechanism maintains a low but non-zero fraction of ionization in the pertinent zones in PPDs, enabling the non-ideal magnetohydrodynamic (MHD) effects to drive disk winds and accretion flows efficiently (Bai & Goodman 2009; Bai 2011, 2017; Wang et al. 2019). Volatile coatings on dust grain surfaces, for example water, regulate grain sintering and thereby shape the dust size distribution throughout PPD evolution (Okuzumi et al. 2016; Hasegawa et al. 2017). Such modulated distributions could influence their interactions with charged particles and lead to the formation of sub-structures in PPDs by alternating the magnetic diffusivities, the key parameters determining the interactions between the magnetic fields and the gas (e.g. Hu et al. 2019, 2021). More generally, the dynamic events related to dust growth, including coagulation, bouncing, breaking, and shattering of grains, are sensitively dependent on the sticking energy between surfaces (Chokshi et al. 1993; Dominik &

Corresponding author: Lile Wang, Shenzhen Xu
 lilew@pku.edu.cn, xushenzhen@pku.edu.cn

Tielens 1997). Such sticking energy should also be susceptible to the conditions on the grain surfaces. Discussions regarding these events are extensive under various circumstances, including theoretical analyses (e.g. Yan et al. 2004; Hirashita & Yan 2009; Ormel et al. 2009; Hirashita & Voshchinnikov 2014), and even experimental studies (Blum 2000).

As the crucial characterization of adsorption processes, the energy of adsorption largely determines the status of volatile species and dust grains themselves in dust-rich astrophysical systems. It is widely assumed, based on observations and experiments, that the astrophysical dust grains can be broadly categorized into silicate grains and carbonaceous grains, whose mass fractions are in the same order of magnitude (see e.g. Jaeger et al. 1994; Dorschner et al. 1995; Jager et al. 1998; Fabian et al. 2000; Henning 2010; see also the data compilations in Draine 2011).

Over the past few decades, the adsorption condition of key species has been measured mainly by experimental studies. These experimental results should, nevertheless, be clarified and specified for their applicability and compatibility. For example, the reported adsorption energy of water on graphite is measured to be $E_{\text{ad}}/k_{\text{B}} \simeq 4800$ K, almost identical to the adsorption on silicates (Sandford & Allamandola 1990; Viti et al. 2004; Bolina et al. 2005; Ilgner & Nelson 2006; Minissale et al. 2022). These values nevertheless seem at odds with the quantum chemistry studies concluding that graphite is only mildly hydrophilic by adsorbing molecules with the van der Waals (vdW hereafter) interactions (see also Ma et al. 2011; Hamada 2012; Brandenburg et al. 2019), while the silicate surfaces could adsorb water mainly by covalent or coordination bonds and hydrogen bonds. Additionally, experimental studies have focused on the single-species adsorption conditions only, while the adsorbates in PPDs could be a mixture of multiple molecular species. The impact of the surface coverage conditions of grains deserve further and more thorough discussions with modern theoretical and computational methods.

In this paper, we will thoroughly study the problems related to the adsorption of molecules via computational chemistry. We will focus on the adsorption of water (H_2O) and carbon monoxide (CO), the most abundant molecules in the PPDs and molecular clouds (other than H_2 and He), onto the representative dust grain surface models, emphasizing the physical pictures of the results and compare them with experiments. This paper is structured as follows. §2 describes the *ab-initio* calculation methods of adsorption on carbonaceous and silicate grains, assuming single and multiple molecule

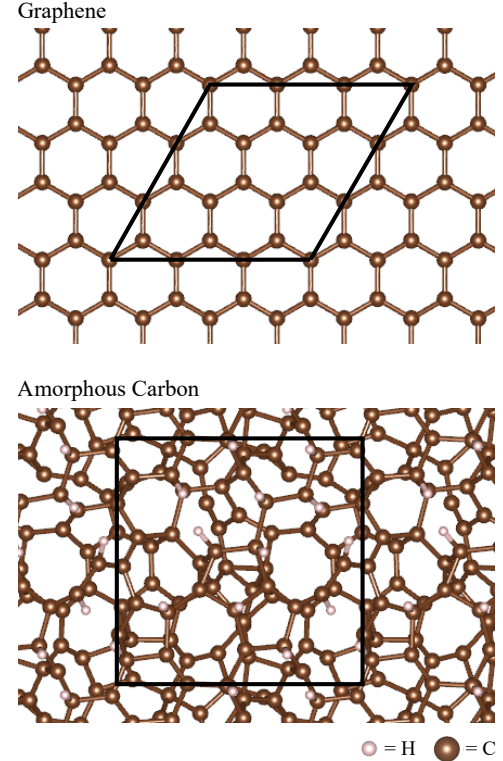


Figure 1. Top-down views of the model carbonaceous substrates studied in this article, including graphene (upper panel) and amorphous carbon (lower panel). The supercells used in the DFT calculations are illustrated by black solid lines in each panel, respectively.

adsorption scenarios. Using these data, §3 evaluates the surface coating conditions of both carbonaceous and silicate dust grains. §5 summarizes the paper, and extends the scope of the results to the gas-phase molecule condensation and sublimation processes onto grain surfaces, the potential impact on planet formation mechanisms.

2. AB-INITIO ADSORPTION ENERGY CALCULATIONS

The condensation process of key molecules onto astrophysical grain surfaces is calculated in this work by examining adsorption conditions using advanced computational chemistry techniques. The *ab-initio* density functional theory (DFT) package VASP (Kresse & Hafner 1993; Kresse & Furthmüller 1996) is adopted, utilizing projector augmented wave (PAW) method calculations with PAW potentials for the atoms involved. To ensure accurate estimations of van der Waals (vdW) interactions, the combination of $r^2\text{SCAN}$ Sun et al. (2015); Furness et al. (2020) and $r\text{VV10}$ Sabatini et al. (2013) functionals is employed for electron exchange-correlation (XC) interactions. This combination, which involves generalized gradient approximations (GGA) and exten-

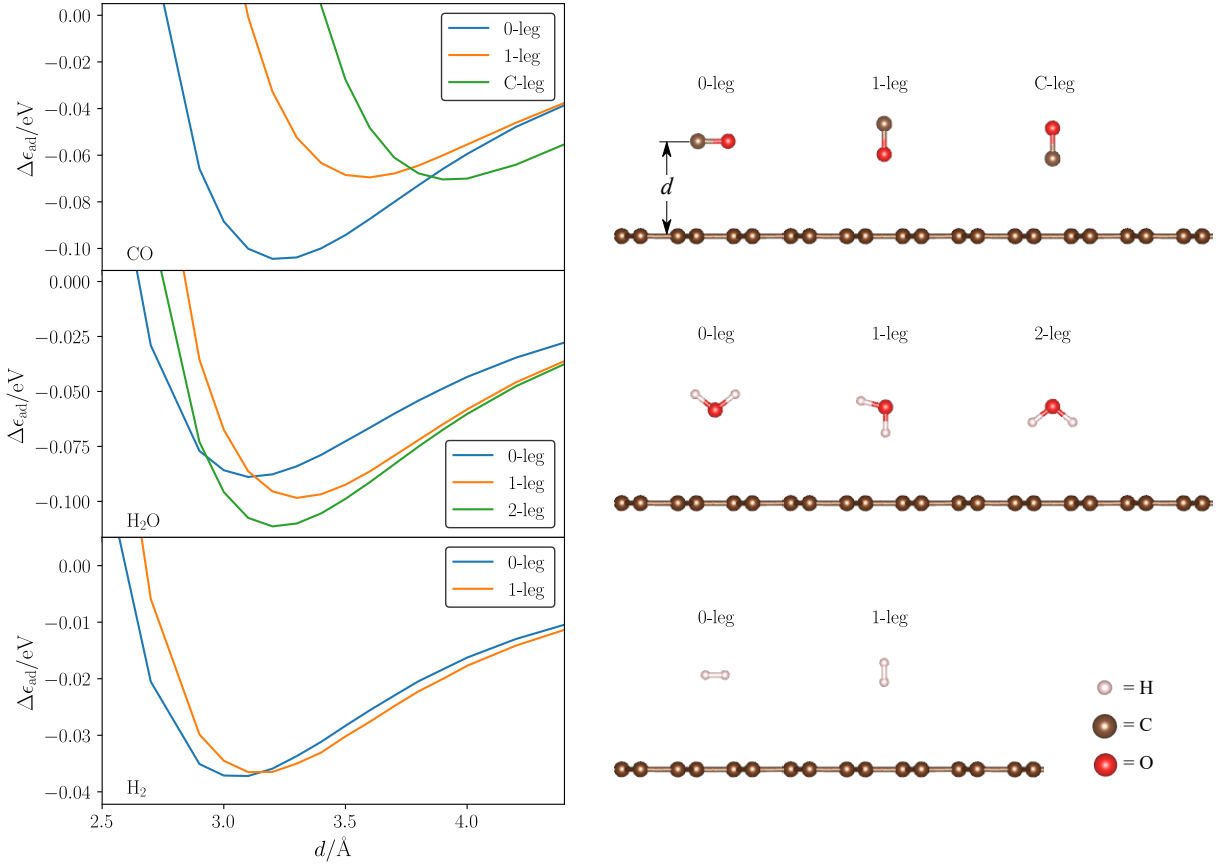


Figure 2. **Left column:** Adsorption energy as functions of molecular orientations and distances to the substrates for CO (upper row), H_2O (middle row), and H_2 (lower row) molecules over graphene substrates. **Right column:** Illustrations of the molecular orientation notations. The depicted molecules correspond to the energy curve panels in the left column.

sions to higher-order derivatives (meta-GGA), is confirmed by various tests and benchmarks (Peng et al. 2016) to handle vdW interactions under the DFT framework accurately in a wide range of situations, especially physisorptions. For instance, the single-molecule physisorption of water onto graphene, which is a highly relevant case to this work, is found to yield an adsorption energy $|\Delta\epsilon_{\text{ad}}| \simeq 0.096$ eV when using r²SCAN+rVV10, a result that is remarkably close to fiducial quantum Monte Carlo (QMC) calculations (Ma et al. 2011; Brandenburg et al. 2019). Within the PAW paradigm, a set of plane-wave bases is utilized to expand the electronic wave functions, with a cutoff energy of 600 eV.

To measure the interaction energy of the systems, the molecule of interest is first positioned at the desired configuration to obtain the total energy with interaction, ϵ_{tot} . The molecule X is then moved sufficiently far from the substrates to ensure that interactions between X and the substrate (as well as neighboring adsorbates, in some cases) became negligible. The DFT calculation is repeated to obtain the sum of the energies of X and the

substrate, $\epsilon_X + \epsilon_{\text{sub}}$. Based on the data collected, the adsorption energy for the given adsorption configuration is subsequently defined as,

$$\Delta\epsilon_{\text{ad}} = \epsilon_X + \epsilon_{\text{sub}} - \epsilon_{\text{tot}}. \quad (1)$$

In cases of adsorption, such convention yields $\Delta\epsilon_{\text{ad}} < 0$. It should be noted that this adsorption energy is derived from the 0 K potential energy surface (PES) without thermodynamic corrections; thus, the results must be adjusted for thermodynamic effects and zero-point energy before application in finite-temperature physical scenarios (Appendix A).

2.1. Adsorption onto Carbonaceous Surfaces

Carbonaceous dust grains are considered to exist in graphitic-like states, including graphites, oxidized graphites, graphene, and even polycyclic aromatic hydrocarbons (PAHs) at the smallest sizes $\lesssim 0.01 \mu\text{m}$ (see also Draine 2011), or as amorphous carbon. In terms of their astrophysical properties, these materials are observed to behave similarly, with the surface layer of car-

bon atoms dominating due to the weak vdW coupling between graphitic layers.

2.1.1. Single-molecule Adsorption onto Graphene

The adsorption of single molecules onto a single layer of graphene and amorphous carbon is first investigated as fiducial cases in this study. Additional calculations are conducted to verify that various situations, such as multiple adsorbates, yield quantitatively consistent results regarding the properties of interest. The construction of the graphene substrate is described in Appendix B.1.

Beginning with water molecules, following Brandenburg et al. (2019), the molecules are positioned above the center of a carbon hexagon, with orientations classified as “0-leg”, “1-leg”, and “2-leg” (illustrated in Figure 2). For each orientation, a series of ΔE_{abs} values is obtained at different displacements d from the substrate surface, measured from the plane of carbon nuclei to the center-of-mass of the adsorbate molecule. It should be noted that during this step, the ionic structure of the system is fixed to manually iterate through configuration space. This setup ensured that the adsorbate configuration—particularly its orientation and distance to the substrates—remained unchanged, allowing correct energy curves to be obtained. The resulting energy curves for these configurations are presented in Figure 2. The difference between our approach (the $r^2\text{SCAN} + r\text{VV10}$ method) and the QMC method for the 1-leg case (Ma et al. 2011) is $\lesssim 0.05$ eV, well within the range of variations among different XC methods (Hamada 2012). Similar calculations for H_2 and CO are performed following the same paradigm, with molecular orientation notations illustrated in Figure 2. For completeness and verification purposes, the adsorption of helium is also examined, yielding an adsorption energy of $|\Delta\epsilon_{\text{ad}}| \lesssim 0.07$ eV.

2.1.2. Adsorption onto amorphous carbon surfaces

The realistic composition of interstellar and protostellar carbonaceous grains is considered to differ considerably from graphites or graphene. According to experimental studies Jager et al. (1998), these grains are more likely to be amorphous carbon, which in various cases may be doped with oxygen and hydrogen at approximately $\sim 1\%$ of atomic concentration. Hydrogen atoms are expected to be located predominantly at grain surfaces due to their inability to achieve coordination numbers greater than unity. Oxygen atoms may exist in both the bulk substrate and near the surface; however, numerical experiments indicate that surface oxygen atoms are always saturated by capturing hydrogen atoms because of intense dipole moments. In practice, while the cases with doped atoms are also calculated,

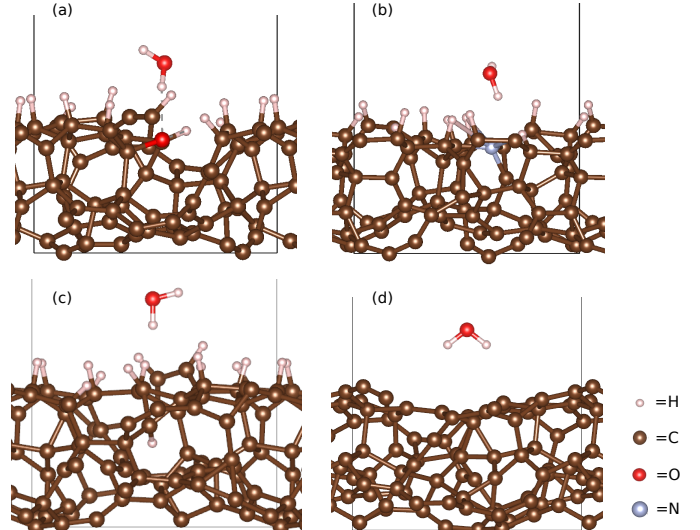


Figure 3. Example of H_2O single-molecule adsorption onto carbonaceous surface under various situations, placed above: (a) “doped” oxygen atom, (b) doped nitrogen atom, (c) hydrogen confined in the bulk substrate, and (d) surface not covered by hydrogen.

only hydrogen and carbon atoms are elaborated and explored in details. The construction of amorphous carbon substrates is explained in Appendix B.2.

Numerical experiments for single-molecule adsorption energy are conducted above the amorphous carbon substrate. The adsorbate is positioned at five different horizontal locations above the surface, with offsets from the horizontal center of the substrate of transverse size $(9.09 \text{ \AA})^2$, as defined by:

$$(\Delta x, \Delta y) \in \{(-1, -1), (-1, 1), (1, -1), (1, 1), (0, 0)\} \times \left(\frac{9.09 \text{ \AA}}{4}, \frac{9.09 \text{ \AA}}{4} \right). \quad (2)$$

At each site, ionic structures are relaxed to locate the energy minimum before the adsorbate is moved sufficiently far from the substrate to evaluate $\Delta\epsilon_{\text{ad}}$ using equation (1). Single-molecule adsorption energies in Table 1 are obtained by averaging $\Delta\epsilon_{\text{ad}}$ over the five sampling sites. It is noted that replacing approximately $\sim 2\%$ of carbon atoms with oxygen yielded nearly identical results, as oxygen atoms are rarely exposed directly (due to hydrogen surface coverage) and thus contributed minimally to interactions with adsorbates. Through deliberate exposure of oxygen and nitrogen atoms at the surface (e.g., Figure 3), the adsorption energy of H_2O via hydrogen bonds is measured to be 0.35 eV (above oxygen) and 0.29 eV (above nitrogen), respectively. The

Table 1. Physical parameters of adsorbates on amorphous carbon grain surfaces.

Adsorbates	Neighbors	ν/THz^\dagger	ξ/THz^\dagger	$ \Delta\epsilon_{\text{ad}} /\text{eV}$ with neighbors		
				0	1	max [‡]
H ₂ O	H ₂ O	~3.5	~2.0	0.16	0.36	0.87
	CO				0.26	0.35
CO	CO	~3.6	~3.0	0.10	0.13	0.14
	H ₂ O				0.24	0.27
H ₂ [*]	H ₂	~5.0	~3.5	0.028	0.029	0.029

NOTE—[†]: The eigen frequencies of vertical (ν) and horizontal (ξ) vibrations of adsorbates on the adsorption sites, estimated by finite difference derivatives.

[‡]: The maximum number of neighbors on the surface is generally 4 nearest and 4 second-nearest.

^{*}: Interactions between H₂ and other types of adsorbates are similarly weak and not presented.

adsorption energy of CO near doping atoms exhibited no significant variations.

When substrate surface coverage fractions become non-negligible, interactions between adsorbates may play a crucial role in modifying their kinetic behaviors. The vdW interactions and hydrogen bonds between adjacent molecules increase the barriers for desorption and hopping, with intensity dependent on both the numbers and types of neighbors. These effects are quantified through numerical experiments based on amorphous carbon substrates. The interaction energy is measured through the following procedures: (1) the adsorbate and its neighbors are placed above the substrate, and ionic configurations are evolved with DFT until stress relaxation, after which the total energy of the relaxed system is evaluated; (2) the adsorbate of interest is moved sufficiently far from the substrate ($\Delta z \gtrsim 10 \text{ \AA}$), and configurations of all remaining atoms are relaxed to reevaluate the total energy.

Energy differences between these steps yielded the “neighbor-enhanced” total binding energy. For tests involving adsorbates with one neighbor, adsorbate pairs are positioned at five different sites (with centers of mass offsets following equation 2) to obtain average enhanced binding energies. The overall binding energy (including adsorption) is observed to increase sub-linearly, as vdW forces exhibit saturation behavior and hydrogen bonds require specific molecular orientations. Tests are also conducted to determine the numbers of different neighbors that maximize absolute binding energy values, beyond which binding energy decreases due to repulsive forces.

2.2. Adsorption onto Silicates

In comparison to carbonaceous grains, silicate compositions are recognized to be considerably more complex. To maintain model tractability while preserving physical relevance, iron-poor enstatite MgSiO₃ (Pnma space group using the Materials Project data, see also Jain et al. 2013) is selected as a proxy for magnesium silicate substrates. This choice is motivated by the abundance of magnesium, which among alkali and alkaline earth metals in the ISM and PPDs, typically matches silicon abundance levels. To emulate astronomical silicate formation conditions, hydrogen atoms are added to exposed oxygen atoms on model silicate surfaces, following procedures analogous to those employed for amorphous carbon. The details of silicate substrate model construction are explained in Appendix B.3.

The specific atomic composition of silicate substrates beneath adsorbate molecules is found to critically determine adsorption properties. Initial investigations positioned molecules with varying orientations at different heights above different atomic sites. After identifying configurations with approximately minimal energy, molecules are placed accordingly on the substrate, and ionic structures are evolved to achieve relaxation, eliminating total stress to the desired accuracy ($\lesssim 10^{-2} \text{ eV \AA}^{-1}$) and thereby locating energy extrema.

Configurations converged at energy extrema are illustrated in Figure 4, with corresponding adsorption energies presented in Table 2. The adsorption energy values for H₂O and CO are generally observed to be one order of magnitude greater than those on carbonaceous surfaces, clearly indicating chemisorption processes. This enhancement is attributed to the coordination numbers of metal centers (Si atoms on (001)[−] and Mg atoms

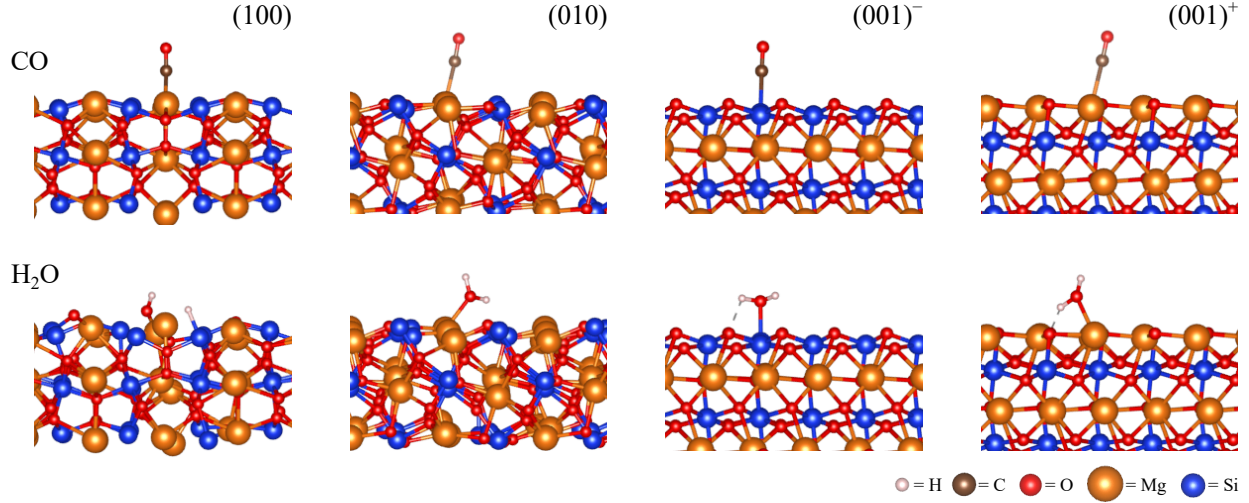


Figure 4. Configurations of adsorbed CO molecules (upper row) and H₂O molecules (lower row) over different crystal surfaces (indicated above each column) of the model silicate MgSiO₃. It should be noted that adsorption of H₂O over the (100) surface results in molecular dissociation.

elsewhere) being significantly less than the saturation value of 6 in bulk MgSiO₃, thereby permitting coordination bond formation and elevating adsorption energies to approximately ~ 1 eV. A notable exception is identified for H₂O adsorption on the (100) surface, where exceptionally high adsorption energy resulted in molecular dissociation.

Chemical bonding is observed to constrain molecular orientations following convergence. In H₂O, the oxygen atom functions as the electron donor, while in CO, the carbon atom serves this role. Given the sufficiently high band intensities and their strong orientation dependence, numerical experiments confirmed that vdW or hydrogen bond interactions between adjacent adsorbates could be neglected on silicate substrates. The increased elasticity resulting from stronger bonds also produced higher eigen frequencies of molecular oscillation (ν and ξ). In contrast, the inability of H₂ to form coordination bonds resulted in negligible adsorption energy.

3. KINETIC MONTE CARLO SIMULATIONS OF GRAIN SURFACES

Surface coverage conditions of dust grains play a fundamental role in regulating coagulation processes through their influence on sticking behavior and surface energy dynamics. To systematically investigate these coverage conditions, we developed a specialized kinetic Monte Carlo (KMC) simulation code, optimized for GPU acceleration to handle the computational demands of these complex simulations⁶ whose general pro-

cedures are explained in Appendix C. It is also noted that the zero-temperature results obtained in §2 need thermodynamic corrections before being applied in the KMC simulations (see Appendix A).

3.1. Setups of KMC simulations

The KMC simulations are implemented on two-dimensional periodic square lattices designed to emulate grain surfaces, where each lattice point corresponds to a discrete adsorption site. This discretization approach allows for efficient modeling of molecular adsorption, desorption, and migration processes across the surface landscape. The KMC framework incorporated both square and hexagonal lattice geometries to assess potential structural dependencies in surface coverage simulations. Comparative analyses revealed that hexagonal lattices produced nearly identical results to square lattices in terms of surface coverage conditions, indicating that the fundamental physical processes governing molecular adsorption exhibit minimal sensitivity to lattice symmetry. Consequently, for enhanced computational efficiency and analytical clarity, only square lattice implementations are retained for detailed presentation and comparative analyses throughout this investigation.

Specific initial and terminal conditions are established to ensure physical relevance and numerical stability. Each simulation commenced with a pre-defined “condensation nucleus” consisting of a 4×4 patch of water molecules positioned on the surface. This initialization strategy prevents numerical artifacts associated with supercooling or superheating conditions that could yield unreliable results. Simulation convergence is defined by

⁶ https://github.com/wll745881210/kmc_ads.

Table 2. Physical parameters of adsorbates on different surfaces of model silicate MgSiO_3 .

Adsorbates	ν/THz	ξ/THz	$ \Delta\epsilon_{\text{ad}} /\text{eV}$ on surfaces			
			(100)	(010)	(001) ⁻	(001) ⁺
H_2O	~ 13	~ 6.0	—**	1.50	1.32	1.17
CO	~ 6.7	~ 5.5	1.23	0.95	0.74	0.45
H_2	~ 6.3	~ 3.0	0.015	0.008	0.016	0.025

NOTE—Similar to Table 1, but the neighbor conditions are not included as the molecules are chemisorbed onto silicate surfaces (see also §2.2).

**: Molecule dissociated after chemisorption.

either the complete disappearance of the condensation nucleus or the achievement of surface coverage exceeding 99%. In cases of extensive coverage, where second and higher molecular layers begin to form, analyses are deliberately restricted to the first monolayer to maintain interpretational clarity.

3.2. Surface coverage conditions simulated by KMC

The divergent surface coating behaviors observed in protoplanetary disks (PPDs) directly originate from the fundamentally different adsorption physics governing carbonaceous and silicate grains. Within a representative PPD model approximating early Solar System conditions, we conduct kinetic Monte Carlo simulations based on vdW-DFT computational results. These KMC implementations comprehensively account for factors influencing desorption rates, including finite-temperature thermodynamic corrections and inter-adsorbate interactions parameterized through the eigen frequencies of adsorbate vibrations (Tables 1 and 2).

Simulations are conducted for dust grains situated in the mid-plane of a model PPD, employing density and temperature profiles consistent with a young stellar object of bolometric luminosity $L \sim 4L_\odot$. The temperature profile follows $T \propto R^{-0.4}$ due to surface flaring effects Chiang & Goldreich (1997), with specific forms given by:

$$T \simeq 280 \text{ K} \left(\frac{R}{\text{AU}} \right)^{-0.4},$$

$$\rho_0 \simeq 3.8 \times 10^{-10} \text{ g cm}^{-3} \left(\frac{R}{\text{AU}} \right)^{-2.8}. \quad (3)$$

This mid-plane density corresponds to a surface density profile of $\Sigma \simeq 600 \text{ g cm}^{-2} (R/\text{AU})^{-1.5}$. Molecular number densities are derived assuming standard abundance ratios: $X(\text{H}_2) \simeq 1$, $X(\text{CO}) \simeq 1.8 \times 10^{-4}$, and $X(\text{H}_2\text{O}) \simeq 1.4 \times 10^{-4}$. Helium atoms are excluded

from consideration due to their negligible adsorption efficiency on grain surfaces.

Across the radial domain of $0.1 < (R/\text{AU}) < 200$, KMC simulations revealed distinct surface coverage patterns for carbonaceous surfaces and the (001)⁻ silicate surface, as illustrated in Figures 5. Silicate surfaces undergo a transition from bare to coated states at $R \lesssim 0.2 \text{ AU}$, a consequence of the substantial chemisorption energies characteristic of CO and H_2O on these substrates. In contrast, KMC results clearly identify a snowline on grain surfaces for water on carbonaceous grains at $R \simeq 8 \text{ AU}$ ($T \simeq 120 \text{ K}$), interior to which surfaces remain uncoated due to elevated thermal energies (Figure 5). This snowline represents a distinct concept from the conventional snowline marking H_2O ice condensation at $T \sim 170 \text{ K}$ (Sasselov & Lecar 2000), with the former being more directly relevant to substrate material coagulation processes. Employing the previously assumed adsorption energy of $\simeq 0.45 \text{ eV}$ would reposition the H_2O snowline at $R \simeq 2 \text{ AU}$.

The fundamental differences in adsorption behavior between carbonaceous and silicate substrates have likely remained obscured in previous research due to systematic misinterpretations of temperature-programmed desorption (TPD) experimental data. This misinterpretation stems from the complex nature of water cluster formation on substrate surfaces. Within water molecule clusters, each molecule typically participates in two hydrogen bonds on average, mirroring the structural configuration of hexagonal ice crystals (I_h). This hydrogen bonding network contributes an internal binding energy of approximately $\epsilon_{\text{hb}} \sim 0.42 \text{ eV}$ per molecule (where the subscript "hb" denotes hydrogen bonds; see also Silverstein et al. (2000)).

Conventional TPD experiments are conducted under conditions substantially different from astrophysical environments: temperatures well below the triple point of water and gas-phase molecule number densities or

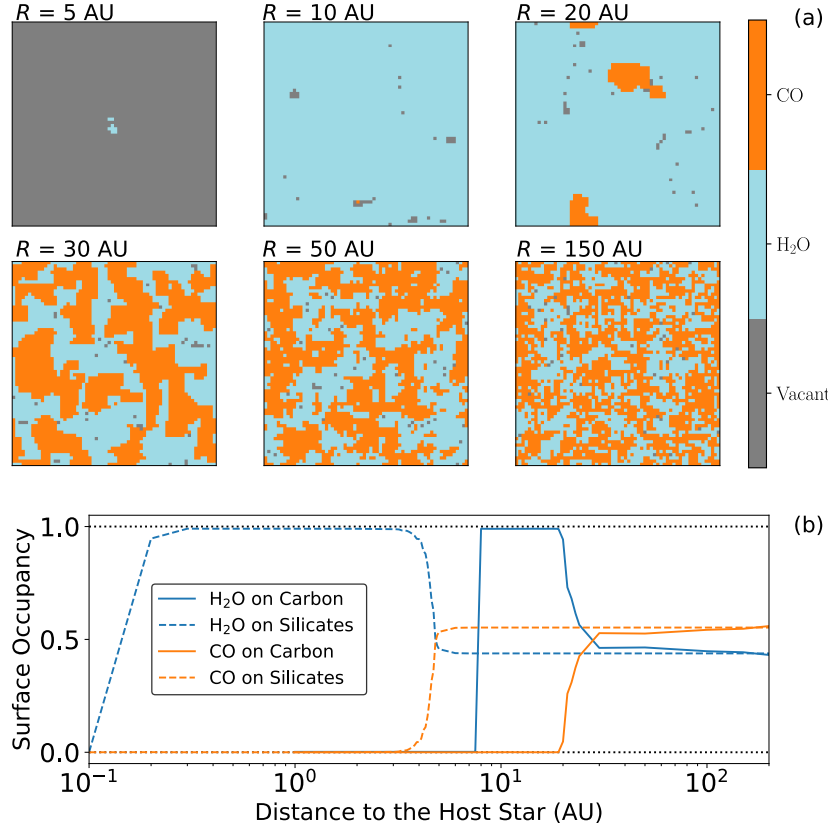


Figure 5. Surface coverage conditions of grains in the mid-plane of a Solar-system-equivalent PPD model. Panel (a) illustrates the coating conditions of amorphous carbon grains given by converged KMC calculations, showing a sample surface with 64×64 site (each site separated by 3 \AA , the typical separation between adsorption sites). Panel (b) plots the surface occupancy conditions for amorphous carbon and the $(001)^+$ surface of MgSiO_3 .

ders of magnitude higher than those found in protoplanetary disks or the interstellar medium. These experimental conditions promote the formation of extensive water clusters on substrate surfaces Leenaarts et al. (2009); Ma et al. (2011); Björneholm et al. (2016). Consequently, molecular addition or removal processes during TPD measurements primarily occur at the interfaces of these water clusters rather than at the actual substrate-adsorbate boundary. This clustering phenomenon could lead to a possible misinterpretation of TPD data: the slopes observed in Arrhenius plots actually reflect $\epsilon_{\text{hb}}/k_{\text{B}}$, the energy scale associated with hydrogen bond breaking, rather than the true substrate adsorption energy $\Delta\epsilon_{\text{ad}}/k_{\text{B}}$. For silicate substrates, the situation is further complicated by the exceptional strength of chemisorption bonds, which remain intact at typical protoplanetary disk temperatures ($T \lesssim 10^3 \text{ K}$). Under these conditions, any molecular desorption processes are governed by hydrogen bond rupture within water clusters, again causing TPD measurements to yield ϵ_{hb} rather than the fundamental substrate adsorption energy. Accurate interpretation of adsorption mechanisms and binding energies is therefore essential for re-

liable modeling of astrophysical processes involving dust grains.

4. DISCUSSIONS

We have combined vdW-corrected *ab-initio* DFT calculations and kinetic Monte Carlo simulations to quantify how key volatiles (H_2O , CO, and H_2) adsorb onto carbonaceous and silicate grain surfaces, and how these material-dependent adsorption energies, combined with KMC simulations, translate into different surface coverage patterns. The results reveal a clear dichotomy between weak physisorption on carbonaceous grains and strong chemisorption on silicates, with important consequences for grain growth and volatile partitioning.

This section places these findings in a broader astrophysical context. We examine how history-dependent initial surface conditions on grains can shift molecular snowline locations (§4.1), investigate how multi-species adsorption, particularly CO– H_2O interactions, modifies CO surface snowlines and gas-phase depletion (§4.2), and connect these processes to molecular condensation and gas-phase depletion, contrasting carbon abundances in different planetary populations, and the ingredients

that should be incorporated into future models of dust evolution and planet formation (§4.3).

4.1. Dependence of snowline locations on evolutionary history

The initial surface conditions of dust grains could be crucial in determining the locations and characteristics of molecular snowlines in protoplanetary disks. When grain surfaces begin with complete H₂O molecular coatings rather than initially bare configurations, the adsorbed water molecules demonstrate significantly enhanced thermal stability due to pre-existing intermolecular binding networks. This phenomenon creates metastable surface conditions that share fundamental physical characteristics with superheating effects observed in other first-order phase transitions.

The enhanced thermal stability arises from the collective binding energy provided by hydrogen bonding networks between adjacent water molecules. These networks create energy barriers that substantially exceed the single-molecule adsorption energy, allowing molecular layers to persist at temperatures far above those predicted by simple adsorption models. Consequently, the ultimate surface coverage conditions and associated gas-phase condensation processes (including potential molecular depletion) become strongly dependent on the specific thermal and dynamical evolution history experienced by dust grains.

The divergence between different evolutionary pathways can be dramatic. When pre-hydrated grains undergo gradual heating from cold initial conditions, they may maintain surface coatings up to temperatures approximately a few tens of Kelvin (typically $\sim 20 - 30$ K) higher than the equivalent snowline temperature for condensation onto initially bare surfaces (not shown in this paper). This effect arises because the formation of new ice layers requires nucleation events that possess significant activation energies, while the removal of existing layers requires overcoming the collective binding energy of the entire molecular network. Therefore, accurate and consistent determination of snowline locations and condensation conditions necessitates comprehensive modeling that incorporates the full thermodynamic history of disk material, including radial drift trajectories and temporal temperature variations. The assumption of instantaneous equilibrium between adsorption and desorption processes proves insufficient for capturing these history-dependent effects, requiring instead the implementation of kinetic models that track the evolutionary pathways of individual grain populations throughout their disk residence.

The final surface coverage of CO on dust grains is not a static property but depends on the specific thermal and dynamical evolution path of the dust population. The initial conditions of grains, such as starting as “dry grains” that are too cold to have undergone significant thermal processing, can preset the availability of binding sites and the efficiency of subsequent ice mantle formation. Furthermore, the radial transport of grains plays a crucial role. Icy grains drifting inward from the outer disk sublimate upon crossing their respective snowlines, temporarily enhancing the local gas-phase abundance before potentially re-condensing onto other grain surfaces under the new thermal conditions.

Consequently, history-dependent snowline locations could vary in different disks, occurring at radii corresponding to different temperatures. Simply inferring their locations based on a fixed temperature (e.g., 20 K for CO) may therefore lead to mismatches. Dust rings and gaps have been found to be nearly ubiquitous in disks. The prevalent hypothesis for their origin is that they are caused by planet–disk interactions (Dong et al. 2015, 2017; Dong & Fung 2017), while the snowline hypothesis (Zhang et al. 2015) has been questioned due to mismatches between the observed ring/gap locations and the expected snowline locations (Long et al. 2018; Bae et al. 2018; van der Marel et al. 2019). Re-examining the connection between the two, while accounting for each disk’s thermal and dynamical history, is therefore needed.

4.2. Impact of multi-species adsorption on CO surface snowlines and gas depletion

The analysis of surface coverage conditions reveals that, based on the disk temperature and hydrodynamic profiles, $R \sim 20$ AU approximately divides the grain surface snowline for CO on amorphous carbon grains, corresponding to a local temperature of $T \simeq 80$ K according to the disk temperature profile defined in equation (3). This temperature appears anomalously high when compared to existing experimental and computational studies, which typically report CO condensation temperatures around ~ 20 K (Cazaux et al. 2017). However, detailed examination of Figure 5 indicates that CO condensation initiation is not an isolated process but rather occurs through coordinated condensation with H₂O molecules.

The underlying mechanism for this elevated condensation temperature becomes evident upon inspection of Table 1, which demonstrates that the interaction energy between a CO molecule and an adjacent H₂O molecule significantly exceeds that between two CO molecules. This enhanced intermolecular binding substantially in-

creases the effective adsorption energy of CO molecules when they are incorporated within a water ice matrix. The resulting configuration resembles “cocrystal” structures, where CO molecules become trapped within the lattice of water ice (distinct from traditional clathrate hydrates, particularly in their interaction characteristics with H₂). This cocrystal formation enables the stabilization of surface-phase CO molecules at temperatures far exceeding their typical triple point, highlighting the critical importance of considering multi-species interactions when modeling gas-phase depletion processes in protoplanetary disks.

It should be further noted that while the primary investigations in this work focus on single-layer adsorption phenomena, additional studies of second-layer H₂O adsorption on silicate-supported water monolayers revealed a single-molecule adsorption energy of 0.28 eV, resulting from the combined effects of hydrogen bonding and van der Waals interactions. When neighbor interactions are incorporated, this corresponds to a “multiple-layer snowline” at ~ 1 AU as indicated by supplementary KMC simulations (not directly illustrated in this work), a finding consistent with conventional snowline scenarios.

Nevertheless, the single-layer adsorption conditions remain particularly relevant for several reasons. First, grain coagulation and subsequent planet formation processes are predominantly governed by single-layer surface conditions, as the sticking versus bouncing outcomes during collisions are primarily determined by center-of-mass collision energies that are most sensitive to the last adsorbed molecular layer. Second, the fundamental physical mechanism enabling CO condensation at elevated temperatures through enhanced binding with H₂O neighbors remains equally valid in multiple-layer scenarios, as the crucial factor is the strengthened binding energy and consequent confinement of CO molecules within the water ice matrix, regardless of the total number of adsorbed layers.

4.3. Molecule Condensation and Gas-Phase Depletion

Our calculations indicate that the CO midplane snowline lies significantly closer to the central star than conventional estimates suggest. In a representative PPD around a solar-type star with $T(1 \text{ AU}) \simeq 150 \text{ K}$, the CO snowline is expected at around 30 AU (e.g., Öberg et al. 2023). When adopting the higher midplane temperature used in our disk model (280 K instead of 150 K at 1 AU), this discrepancy becomes even more pronounced. This inward shift of CO snowline in our model mainly arises from enhanced CO–H₂O binding, which promotes earlier condensation of CO onto water-rich grain surfaces.

Observationally, molecular snowline locations can be inferred from chemical tracers of gas-phase abundances, such as N₂H⁺ for CO, which usually place the CO snowline beyond 40 AU in disks around solar-type stars (Qi et al. 2013, 2019). However, these diagnostics are not always uniquely linked to volatile depletion at the corresponding snowline and can be affected by optical depth effects, non-thermal desorption, or chemical processing (van ’t Hoff et al. 2017). These measurements typically trace the traditional 20 K condensation front, where the CO gas abundance drops dramatically. In contrast, our models predict the onset of CO condensation significantly closer to the star, at a region not directly captured by such observations. This suggests that a substantial disk region may contain partially CO-ice-coated grains, effectively extending the CO-ice zone inward compared to classical estimates.

This expanded CO-ice zone has important implications for the discrepancy between CO-based gas mass estimates and other disk mass tracers. Early ALMA observations have often inferred surprisingly low gas disk masses under the standard assumption of a CO–H₂ ratio of 10^{-4} (e.g. Miotello et al. 2017; Long et al. 2017). These estimates often yield total gas masses below one Jupiter mass for disks only a few Myr old, implying that giant planet formation must terminate very early. One proposed solution is that current thermochemical models underestimate CO depletion, thereby underpredicting CO line fluxes. Indeed, models incorporating grain-surface chemistry and CO conversion into CO₂ ices can produce higher apparent gas masses (Ruaud et al. 2022). However, such models still fail to fully resolve the discrepancy; for example, the CO-based gas mass estimate for IM Lup remains an order of magnitude lower than its dynamical disk mass (Deng et al. 2025). Our results should therefore be incorporated in future models to improve the accuracy of disk mass determinations, a key parameter for disk evolution and planet formation models.

Our models also predict that H₂O ice can sublime at lower temperatures and thus at larger disk radii, when it is coated on carbonaceous grains. These shifts of snowline locations have important implications for interpreting the inner disk chemistry revealed by JWST MIR spectra. The initial gas-phase C/O ratio in disks is largely determined by the relative positions of major volatile snowlines. For example, it is expected to be lower inside the H₂O snowline than in the region between H₂O and CO snowlines (Öberg et al. 2011). Current interpretations of JWST spectra often invoke the sublimation of icy grains as they drift inward and cross various snowlines (e.g., Mah et al. 2023). Recent

models that include CO entrapment in water ice suggest elevated C/O and C/H ratio inside the water snowline, by up to a factor of 10 over 1 Myr (Williams et al. 2025). This process is analogous to the closer-in onset of CO condensation predicted in our calculations. Precise knowledge of snowline locations and their temperature dependencies is thus essential for modeling disk chemistry. The outward shift of the water snowline predicted here adds an additional layer of complexity that future chemo-dynamical models should consider. Moreover, the lower sublimation temperature of water ice implies that H₂O vapor may persist at colder temperatures, motivating future far-infrared observations with facilities such as PRIMA to probe water beyond the canonical snowline.

5. SUMMARY

We have combined vdW-corrected *ab-initio* DFT calculations (§2) and kinetic Monte Carlo simulations (§3) to quantify how key volatiles (H₂O, CO, and H₂) adsorb onto carbonaceous and silicate grain surfaces. The resulting, material-dependent adsorption energies, when propagated through the KMC framework, produce distinct surface coverage patterns and well-defined snowlines on grain surfaces in a representative protoplanetary disk model (Figure 5). Our calculations also demonstrate a clear dichotomy between weak physisorption on carbonaceous grains and strong chemisorption on silicates (Tables 1 and 2), which causes carbonaceous grains to lose their volatile coatings in the inner disk while silicates remain molecularly coated over a much wider range of radii.

Building on this physical picture, we show that history-dependent initial surface conditions and evolu-

tionary paths can shift snowline locations (§4.1), that multi-species adsorption and enhanced CO binding in H₂O-rich ices can move the effective CO surface snowline inward and strengthen gas-phase CO depletion (§4.2), and that these effects together impact disk gas-mass estimates, the interpretation of snowline-sensitive tracers, and JWST spectra in planet-forming disks (§4.3).

From an observational perspective, the carbonaceous snowline on carbonaceous grain surfaces developed in this work should influence carbon abundance patterns in extrasolar planetary systems, as the lack of “glue molecules” on carbonaceous grains at warm temperatures can lead to the generic scarcity of carbon in regions closer to the host star. Future observational campaigns, particularly those utilizing improved characterization of elemental abundances in exoplanetary atmospheres, will provide crucial tests of these predictions across a broader range of planetary system architectures. Such data may additionally offer constraints on potential planetary migration histories. This work establishes a foundation for investigating key astrophysical processes through a modernized approach grounded in the fundamental physics of molecules, atoms, and electrons, bridging microscopic interactions with macroscopic astrophysical phenomena.

ACKNOWLEDGMENTS

This work is supported by the NSFC General Project 12573067. This research was enabled partially by the High-performance Computing Platform of Peking University. We thank our colleagues: Di Li, Luis C. Ho, Jeremy Goodman, Ahmad Nemer, Satoshi Okuzumi, Kengo Tomida, Kazuyuki Omukai, Mordecai Mac-Low, Xiao Hu, Siyi Feng, for helpful discussions and comments.

APPENDIX

A. THERMODYNAMIC CORRECTIONS FOR ADSORPTION ENERGIES

The thermodynamic treatment of adsorbate-substrate systems requires careful consideration of their inherent complexity compared to isolated molecular systems. Dust grain substrates possess substantially larger heat capacities than individual adsorbate molecules and maintain stiff thermal equilibrium with the diffuse radiation fields characteristic of interstellar media and protoplanetary disks Chiang & Goldreich (1997). Consequently, these substrates effectively function as isothermal heat reservoirs during adsorption-desorption pro-

cesses. When molecular desorption occurs, the thermal relaxation timescale in the gas phase through collisions with other molecules can be estimated following Draine (2011):

$$\begin{aligned} \tau_{\text{coll,gas}} &\equiv [n_{\text{H}_2} \langle \sigma v_{\text{th}} \rangle]^{-1} \\ &\sim 1 \text{ s} \times \left(\frac{T}{10^2 \text{ K}} \right)^{-1/2} \left(\frac{\rho_{\text{gas}}}{10^{-14} \text{ g cm}^{-3}} \right)^{-1/2}. \end{aligned} \quad (\text{A1})$$

Under typical protoplanetary disk mid-plane conditions, $\tau_{\text{coll,gas}}$ exceeds the desorption timescale by more than ten orders of magnitude, effectively halting thermal en-

ergy exchange between desorbed molecules and the surrounding gas phase. This dramatic timescale separation necessitates distinct thermodynamic treatments for different molecular degrees of freedom: molecular motion perpendicular to the substrate surface (the desorption direction) should be treated as adiabatic, with the internal energy change $\Delta\epsilon_{\text{ad}}$ serving as the relevant thermodynamic potential. Conversely, motion parallel to the surface maintains continuous thermal contact with the substrate heat reservoir, requiring that interactions with neighboring adsorbates during hopping and desorption processes be treated isothermally.

The vibrational characteristics of adsorbed molecules were determined through analysis of their quasi-harmonic oscillations near energy minima. Following convergence to minimal energy configurations with fixed substrate ionic structures, the VASP software package was employed to evaluate second derivatives of the potential energy surface via finite differences. Diagonalization of the resulting Hessian matrices yielded eigenfrequencies for adsorbate oscillation modes, enabling precise thermodynamic corrections.

For the adiabatic dimension (perpendicular motion), thermodynamic corrections primarily account for the transition from free translational motion to confined quasi-harmonic oscillations. The internal energy correction incorporating zero-point energy (ZPE) contributions is given by:

$$\delta\epsilon_{\perp} = h\nu \left(\frac{1}{2} + \frac{1}{e^{\beta h\nu} - 1} \right) - \frac{1}{2}k_{\text{B}}T, \quad (\text{A2})$$

where ν represents the vertical eigenfrequencies tabulated in Tables 1 and 2, and $\beta \equiv (k_{\text{B}}T)^{-1}$.

For the isothermal dimensions (parallel motion), the Helmholtz free energy serves as the appropriate thermodynamic potential. The binding energy correction is derived from the free energy difference between the bounded oscillatory state and the unbounded translational state:

$$\begin{aligned} f_{\text{osci}} &= \frac{h\xi}{2} + \frac{1}{\beta} \ln [1 - e^{-\beta h\xi}] , \\ f_{\text{trans}} &= -\frac{2}{\beta} \ln \left[\delta l \left(\frac{h^2 \beta}{2\pi\mu} \right)^{-1/2} \right] , \end{aligned} \quad (\text{A3})$$

where ξ denotes the horizontal eigenfrequencies from Tables 1 and 2, μ represents the molecular mass, and $\lambda_{\text{th}} \equiv (h^2\beta/2\pi\mu)^{1/2}$ corresponds to the thermal de Broglie wavelength. The parameter δl describes the average intermolecular distance on the substrate surface, which varies with both gas-phase and adsorbed-phase conditions. For computational simplicity, $\delta l \sim 10$ was adopted, approximately corresponding to the distance

where interactions between adjacent adsorbates become negligible. The logarithmic dependence on δl ensures that the results remain insensitive to its exact value, requiring only order-of-magnitude accuracy. Increasing δl elevates the value of δf_{\parallel} , thereby generally weakening the binding between adsorbates.

B. CONSTRUCTION OF DUST GRAIN SUBSTRATE MODELS

B.1. Graphene Substrate Construction

The potential energy surface (PES) for molecular adsorption was systematically characterized through computational mapping of adsorption energy curves for H_2O , CO , and H_2 using a single-layer graphene sheet as the model substrate. A 3×3 supercell configuration was employed, comprising 18 carbon atoms arranged in a diamond-shaped lattice with dimensions $7.40 \text{ \AA} \times 7.40 \text{ \AA}$ and an open angle of $\pi/3$. To eliminate spurious interactions between periodic images, a vacuum space of 25 \AA was maintained above the graphene surface. Adsorbate molecules were systematically positioned at varying distances from the substrate surface to sample the complete adsorption potential landscape.

Brillouin zone sampling was conducted using a Γ -centered $1 \times 1 \times 1$ k -point grid during initial DFT calculations. The adequacy of this sampling scheme was verified through comparative tests employing denser $3 \times 3 \times 1$ and $5 \times 5 \times 1$ k -point meshes at identified energy minima, confirming numerical reliability and convergence of the computed adsorption energies. Following initial energy curve determination, full structural relaxation of adsorbate configurations was performed to locate the true energy minima and obtain accurate minimal adsorption energies.

B.2. Amorphous Carbon Substrate Construction

A representative model for interstellar amorphous carbon grains was constructed through a multi-step computational procedure. Initial configuration generation involved placement of 75 carbon atoms on a randomly perturbed $5 \times 5 \times 3$ lattice within a periodic boundary condition unit cell. To emulate the hydrogenation conditions expected in interstellar environments, 30 hydrogen atoms were randomly distributed atop the carbon bulk, preferentially associating with carbon atoms exhibiting low coordination numbers.

Structural optimization was performed using DFT with full consideration of electronic interactions, allowing both ionic positions and supercell dimensions to vary during relaxation. Convergence was achieved when the total force on all atoms fell below the threshold of $10^{-2} \text{ eV \AA}^{-1}$. Hydrogen atoms failing to form chemi-

cal bonds with carbon during this process were subsequently removed from the system, simulating the natural saturation processes occurring in astrophysical environments.

The final optimized structure possessed a supercell with transverse dimensions of $(9.09 \text{ \AA})^2$ and exhibited a mixed hybridization state distribution: 47% of carbon atoms in sp^2 configuration and 53% in sp^3 configuration. The resulting carbon bulk demonstrated an average thickness of $\sim 5.1 \text{ \AA}$ and a density of $\sim 2.4 \text{ g cm}^{-3}$, values consistent with experimentally characterized amorphous carbon materials. Surface hydrogen coverage reached $\sim 0.16 \text{ cm}^{-2}$, corresponding to approximately 1% atomic hydrogen concentration for a spherical grain of radius $0.05 \mu\text{m}$, in excellent agreement with experimental measurements [Jager et al. \(1998\)](#).

B.3. Silicate Substrate Construction

Model silicate substrates were constructed using iron-poor enstatite MgSiO_3 in the Pnma space group as a representative magnesium silicate system. Surface selection presented significant complexity due to the theoretically infinite variety of possible crystal facet orientations. To ensure computational tractability while maintaining physical relevance, surfaces with the lowest Miller indices, (100), (010), and (001), were selected as representative substrates. Surface terminations were specifically chosen to minimize dipole moments in the near-surface region, enhancing numerical stability and physical realism.

The (001) surface orientation exhibited particular complexity, manifesting two distinct termination types: the $(001)^+$ surface exposing magnesium atoms and the $(001)^-$ surface exposing silicon atoms. This directional asymmetry resulted from the non-centrosymmetric nature of the Pnma crystal structure. In contrast, the (100) and (010) surfaces did not exhibit such directional dependence due to inherent symmetry properties.

Supercell dimensions were carefully optimized for each surface orientation: $(9.96 \text{ \AA} \times 13.96 \text{ \AA})$ for the (100) surface, $(9.66 \text{ \AA} \times 13.96 \text{ \AA})$ for the (010) surface, and $(9.66 \text{ \AA} \times 9.96 \text{ \AA})$ for both $(001)^{\pm}$ surfaces. A consistent vacuum thickness of 20 \AA was maintained above all surfaces to prevent artificial interactions between periodic images and ensure accurate simulation of isolated surface-adsorbate systems.

C. GENERAL PROCEDURES OF KMC SIMULATIONS

KMC simulations have been performed extensively for various studies for surface physical and chemical proper-

ties (e.g. [Andersen et al. 2019](#)). Three distinct processes are modeled to occur on the simulated grain surfaces, each characterized by specific rate equations:

Adsorption. Each unoccupied surface site experiences molecular adsorption at a characteristic rate defined by $\zeta_i \equiv n_i v_{\text{th},i} \Sigma$, representing the effective incoming flux frequency for molecular species i . This formulation incorporates the gas-phase number density n_i , the thermal velocity $v_{\text{th},i}$ derived from Maxwell-Boltzmann statistics, and Σ , which denotes the effective adsorption cross-section with intrinsic sticking probability implicitly included. Through systematic analysis of solid-phase structures derived from vdW-DFT calculations, an optimal value of $\Sigma \simeq (3 \text{ \AA})^2$ is determined, providing a consistent approximation applicable across all substrate-adsorbate combinations examined in this study.

Hopping. Molecular migration across surface sites is modeled through a hopping mechanism, where an adsorbate occupying a site with N adjacent vacancies exhibits a hopping rate expressed as:

$$k_{\text{hop}} \simeq N \xi \exp \left[\frac{\sum (\Delta \epsilon_{\text{hop}} + f_{\text{osci}}) - f_{\text{trans}}}{k_B T} \right], \quad (\text{C4})$$

The summation encompasses all neighboring sites, while f_{osci} and f_{trans} represent the free energy contributions from oscillatory and translational motions, respectively, as defined in equation (A3). For carbonaceous substrates, the hopping energy barrier $\Delta \epsilon_{\text{hop}} > 0$ induced by each neighbor is quantified through the energy difference between adsorption configurations with zero and one neighbors, as tabulated in Table 1. In contrast, silicate substrates exhibited significantly weaker inter-adsorbate interactions relative to their substantial chemisorption energies, permitting the approximation of the hopping barrier simply by the absolute adsorption energy $|\Delta \epsilon_{\text{ad}}|$.

Desorption. Molecular detachment from surface sites is characterized by a desorption rate governed by the expression:

$$k_{\text{des}} \simeq \nu \exp \left(\frac{\Delta \epsilon_{\text{ad}} + \delta \epsilon_{\perp} - f_{\text{trans}}}{k_B T} \right), \quad (\text{C5})$$

where the vibrational frequency ν of adsorbed molecules corresponds to the parameter defined in equation (A2). The desorption energy barrier $\Delta \epsilon_{\text{ad}}$ is computed using adsorption energies from Tables 1 and 2, with appropriate adjustments accounting for both the quantity and chemical identity of neighboring adsorbates to accurately capture cooperative effects in molecular binding.

REFERENCES

Ádámkovics, M., Glassgold, A. E., & Najita, J. R. 2014, *Astrophysical Journal*, 786, 135, doi: [10.1088/0004-637X/786/2/135](https://doi.org/10.1088/0004-637X/786/2/135)

Andersen, M., Panosetti, C., & Reuter, K. 2019, *Frontiers in Chemistry*, 7, 202, doi: [10.3389/fchem.2019.00202](https://doi.org/10.3389/fchem.2019.00202)

Bae, J., Pinilla, P., & Birnstiel, T. 2018, *ApJ*, 864, L26, doi: [10.3847/2041-8213/aadd51](https://doi.org/10.3847/2041-8213/aadd51)

Bai, X.-N. 2011, *Astrophysical Journal*, 739, 51, doi: [10.1088/0004-637X/739/1/51](https://doi.org/10.1088/0004-637X/739/1/51)

—. 2017, *Astrophysical Journal*, 845, 75, doi: [10.3847/1538-4357/aa7dda](https://doi.org/10.3847/1538-4357/aa7dda)

Bai, X.-N., & Goodman, J. 2009, *Astrophysical Journal*, 701, 737

Björneholm, O., Hansen, M. H., Hodgson, A., et al. 2016, *Chemical reviews*, 116, 7698

Blum, J. 2000, *Space Science Reviews*, 92, 265, doi: [10.1023/A:1005251414391](https://doi.org/10.1023/A:1005251414391)

Bolina, A. S., Wolff, A. J., & Brown, W. A. 2005, *Journal of Chemical Physics*, 109, 016836–016845, doi: [10.1021/jp0528111](https://doi.org/10.1021/jp0528111)

Brandenburg, J. G., Zen, A., Fitzner, M., et al. 2019, *The journal of physical chemistry letters*, 10, 358

Cazaux, S., Martín-Doménech, R., Chen, Y. J., Muñoz Caro, G. M., & González Díaz, C. 2017, *Astrophysical Journal*, 849, 80, doi: [10.3847/1538-4357/aa8b0c](https://doi.org/10.3847/1538-4357/aa8b0c)

Cazaux, S., & Tielens, A. G. G. M. 2002, *Astrophysical Journal*, 575, L29, doi: [10.1086/342607](https://doi.org/10.1086/342607)

—. 2004, *Astrophysical Journal*, 604, 222, doi: [10.1086/381775](https://doi.org/10.1086/381775)

Chiang, E. I., & Goldreich, P. 1997, *Astrophysical Journal*, 490, 368, doi: [10.1086/304869](https://doi.org/10.1086/304869)

Chokshi, A., Tielens, A. G. G. M., & Hollenbach, D. 1993, *Astrophysical Journal*, 407, 806, doi: [10.1086/172562](https://doi.org/10.1086/172562)

Deng, D., Gorti, U., Pascucci, I., & Ruaud, M. 2025, arXiv e-prints, arXiv:2509.15487, doi: [10.48550/arXiv.2509.15487](https://doi.org/10.48550/arXiv.2509.15487)

Dominik, C., & Tielens, A. G. G. M. 1997, *Astrophysical Journal*, 480, 647, doi: [10.1086/303996](https://doi.org/10.1086/303996)

Dong, R., & Fung, J. 2017, *ApJ*, 835, 146, doi: [10.3847/1538-4357/835/2/146](https://doi.org/10.3847/1538-4357/835/2/146)

Dong, R., Li, S., Chiang, E., & Li, H. 2017, *ApJ*, 843, 127, doi: [10.3847/1538-4357/aa72f2](https://doi.org/10.3847/1538-4357/aa72f2)

Dong, R., Zhu, Z., & Whitney, B. 2015, *ApJ*, 809, 93, doi: [10.1088/0004-637X/809/1/93](https://doi.org/10.1088/0004-637X/809/1/93)

Dorschner, J., Begemann, B., Henning, T., Jaeger, C., & Mutschke, H. 1995, *Astronomy and Astrophysics*, 300, 503

Draine, B. T. 2011, *Physics of the Interstellar and Intergalactic Medium* (Princeton University Press)

Fabian, D., Jäger, C., Henning, T., Dorschner, J., & Mutschke, H. 2000, *Astronomy and Astrophysics*, 364, 282

Furness, J. W., Kaplan, A. D., Ning, J., Perdew, J. P., & Sun, J. 2020, *The journal of physical chemistry letters*, 11, 8208

Hamada, I. 2012, *Physical Review B*, 86, 195436

Hasegawa, Y., Okuzumi, S., Flock, M., & Turner, N. J. 2017, *Astrophysical Journal*, 845, 31, doi: [10.3847/1538-4357/aa7d55](https://doi.org/10.3847/1538-4357/aa7d55)

Henning, T. 2010, *Annual Review of Astronomy and Astrophysics*, 48, 21, doi: [10.1146/annurev-astro-081309-130815](https://doi.org/10.1146/annurev-astro-081309-130815)

Hirashita, H., & Voshchinnikov, N. V. 2014, *Monthly Notices of the Royal Astronomical Society*, 437, 1636, doi: [10.1093/mnras/stt1997](https://doi.org/10.1093/mnras/stt1997)

Hirashita, H., & Yan, H. 2009, *Monthly Notices of the Royal Astronomical Society*, 394, 1061, doi: [10.1111/j.1365-2966.2009.14405.x](https://doi.org/10.1111/j.1365-2966.2009.14405.x)

Hu, X., Wang, L., Okuzumi, S., & Zhu, Z. 2021, *Astrophysical Journal*, 913, 133, doi: [10.3847/1538-4357/abf4c7](https://doi.org/10.3847/1538-4357/abf4c7)

Hu, X., Zhu, Z., Okuzumi, S., et al. 2019, *Astrophysical Journal*, 885, 36, doi: [10.3847/1538-4357/ab44cb](https://doi.org/10.3847/1538-4357/ab44cb)

Ilgner, M., & Nelson, R. P. 2006, *Astronomy and Astrophysics*, 445, 205, doi: [10.1051/0004-6361:20053678](https://doi.org/10.1051/0004-6361:20053678)

Jaeger, C., Mutschke, H., Begemann, B., Dorschner, J., & Henning, T. 1994, *Astronomy and Astrophysics*, 292, 641

Jager, C., Mutschke, H., & Henning, T. 1998, *Astronomy and Astrophysics*, 332, 291

Jain, A., Ong, S. P., Hautier, G., et al. 2013, *APL Materials*, 1, 011002, doi: [10.1063/1.4812323](https://doi.org/10.1063/1.4812323)

Kresse, G., & Furthmüller, J. 1996, *Phys. Rev. B*, 54, 11169, doi: [10.1103/PhysRevB.54.11169](https://doi.org/10.1103/PhysRevB.54.11169)

Kresse, G., & Hafner, J. 1993, *Phys. Rev. B*, 47, 558, doi: [10.1103/PhysRevB.47.558](https://doi.org/10.1103/PhysRevB.47.558)

Leenaerts, O., Partoens, B., & Peeters, F. M. 2009, *Phys. Rev. B*, 79, 235440, doi: [10.1103/PhysRevB.79.235440](https://doi.org/10.1103/PhysRevB.79.235440)

Long, F., Herczeg, G. J., Pascucci, I., et al. 2017, *ApJ*, 844, 99, doi: [10.3847/1538-4357/aa78fc](https://doi.org/10.3847/1538-4357/aa78fc)

Long, F., Pinilla, P., Herczeg, G. J., et al. 2018, *ApJ*, 869, 17, doi: [10.3847/1538-4357/aae8e1](https://doi.org/10.3847/1538-4357/aae8e1)

Ma, J., Michaelides, A., Alfè, D., et al. 2011, *Phys. Rev. B*, 84, 033402, doi: [10.1103/PhysRevB.84.033402](https://doi.org/10.1103/PhysRevB.84.033402)

Mah, J., Bitsch, B., Pascucci, I., & Henning, T. 2023, *A&A*, 677, L7, doi: [10.1051/0004-6361/202347169](https://doi.org/10.1051/0004-6361/202347169)

Minissale, M., Aikawa, Y., Bergin, E., et al. 2022, *ACS Earth and Space Chemistry*, 6, 597, doi: [10.1021/acsearthspacechem.1c00357](https://doi.org/10.1021/acsearthspacechem.1c00357)

Miotello, A., van Dishoeck, E. F., Williams, J. P., et al. 2017, *A&A*, 599, A113, doi: [10.1051/0004-6361/201629556](https://doi.org/10.1051/0004-6361/201629556)

Öberg, K. I., Facchini, S., & Anderson, D. E. 2023, *ARA&A*, 61, 287, doi: [10.1146/annurev-astro-022823-040820](https://doi.org/10.1146/annurev-astro-022823-040820)

Öberg, K. I., Murray-Clay, R., & Bergin, E. A. 2011, *ApJ*, 743, L16, doi: [10.1088/2041-8205/743/1/L16](https://doi.org/10.1088/2041-8205/743/1/L16)

Okuzumi, S., Momose, M., Sirono, S.-i., Kobayashi, H., & Tanaka, H. 2016, *Astrophysical Journal*, 821, 82, doi: [10.3847/0004-637X/821/2/82](https://doi.org/10.3847/0004-637X/821/2/82)

Ormel, C. W., Paszun, D., Dominik, C., & Tielens, A. G. G. M. 2009, *Astronomy and Astrophysics*, 502, 845, doi: [10.1051/0004-6361/200811158](https://doi.org/10.1051/0004-6361/200811158)

Peng, H., Yang, Z.-H., Perdew, J. P., & Sun, J. 2016, *Phys. Rev. X*, 6, 041005, doi: [10.1103/PhysRevX.6.041005](https://doi.org/10.1103/PhysRevX.6.041005)

Qi, C., Öberg, K. I., Wilner, D. J., et al. 2013, *Science*, 341, 630, doi: [10.1126/science.1239560](https://doi.org/10.1126/science.1239560)

Qi, C., Öberg, K. I., Espaillat, C. C., et al. 2019, *ApJ*, 882, 160, doi: [10.3847/1538-4357/ab35d3](https://doi.org/10.3847/1538-4357/ab35d3)

Ruaud, M., Gorti, U., & Hollenbach, D. J. 2022, *ApJ*, 925, 49, doi: [10.3847/1538-4357/ac3826](https://doi.org/10.3847/1538-4357/ac3826)

Sabatini, R., Gorni, T., & de Gironcoli, S. 2013, *Phys. Rev. B*, 87, 041108, doi: [10.1103/PhysRevB.87.041108](https://doi.org/10.1103/PhysRevB.87.041108)

Sandford, S. A., & Allamandola, L. J. 1990, *Icarus*, 87, 188, doi: [10.1016/0019-1035\(90\)90028-8](https://doi.org/10.1016/0019-1035(90)90028-8)

Sasselov, D. D., & Lecar, M. 2000, *Astrophysical Journal*, 528, 995, doi: [10.1086/308209](https://doi.org/10.1086/308209)

Silverstein, K. A., Haymet, A., & Dill, K. A. 2000, *Journal of the American Chemical Society*, 122, 8037

Sun, J., Ruzsinszky, A., & Perdew, J. P. 2015, *Phys. Rev. Lett.*, 115, 036402, doi: [10.1103/PhysRevLett.115.036402](https://doi.org/10.1103/PhysRevLett.115.036402)

van der Marel, N., Dong, R., di Francesco, J., Williams, J. P., & Tobin, J. 2019, *ApJ*, 872, 112, doi: [10.3847/1538-4357/aaf31](https://doi.org/10.3847/1538-4357/aaf31)

van 't Hoff, M. L. R., Walsh, C., Kama, M., Facchini, S., & van Dishoeck, E. F. 2017, *A&A*, 599, A101, doi: [10.1051/0004-6361/201629452](https://doi.org/10.1051/0004-6361/201629452)

Viti, S., Collings, M. P., Dever, J. W., McCoustra, M. R. S., & Williams, D. A. 2004, *Monthly Notices of the Royal Astronomical Society*, 354, 1141, doi: [10.1111/j.1365-2966.2004.08273.x](https://doi.org/10.1111/j.1365-2966.2004.08273.x)

Wang, L., Bai, X.-N., & Goodman, J. 2019, *Astrophysical Journal*, 874, 90, doi: [10.3847/1538-4357/ab06fd](https://doi.org/10.3847/1538-4357/ab06fd)

Williams, J., Krijt, S., Bitsch, B., Houge, A., & Bergner, J. 2025, *MNRAS*, doi: [10.1093/mnras/staf1839](https://doi.org/10.1093/mnras/staf1839)

Yan, H., Lazarian, A., & Draine, B. T. 2004, *Astrophysical Journal*, 616, 895, doi: [10.1086/425111](https://doi.org/10.1086/425111)

Zhang, K., Blake, G. A., & Bergin, E. A. 2015, *ApJ*, 806, L7, doi: [10.1088/2041-8205/806/1/L7](https://doi.org/10.1088/2041-8205/806/1/L7)